Improving Fast Ripples Recording With Model-Guided Design of Microelectrodes

M. Al Harrach, G. Dauly, H. Seyedeh-Mousavi, G. Dieuset, P. Benquet, E. Ismailova, F. Wendling

To cite this version:

M. Al Harrach, G. Dauly, H. Seyedeh-Mousavi, G. Dieuset, P. Benquet, et al.. Improving Fast Ripples Recording With Model-Guided Design of Microelectrodes. IEEE Transactions on Biomedical Engineering, 2023, 70 (8), pp.2496-2505. 10.1109/TBME.2023.3250763 . hal-04192094

HAL Id: hal-04192094
https://hal.science/hal-04192094

Submitted on 8 Sep 2023

This article has been accepted for publication in IEEE Transactions on Biomedical Engineering. This is the author's version which has not been fully edited and content may change prior to final publication. Citation information: DOI 10.1109/TBME.2023.3250763

Improving Fast Ripples Recording with Model-Guided Design of Microelectrodes

M. Al Harrach, G. Dauly, H. Seyedeh-Mousavi, G. Dieuset, P. Benquet, E. Ismailova and F. Wendling

***Abstract*— *Objective*: Microelectrodes allow for the recording of neural activities with a high spatial resolution. However, their small sizes result in high impedance causing high thermal noise and poor signal-to-noise ratio. In drug-resistant epilepsy, the accurate detection of Fast Ripples (FRs; 250-600 Hz) can help in the identification of epileptogenic networks and Seizure Onset Zone (SOZ). Consequently, good-quality recordings are instrumental to improve surgical outcome. In this work, we propose a novel model-based approach for the design of microelectrodes optimized for FRs recording. *Methods*: A 3D microscale computational model was developed to simulate FRs generated in the hippocampus (CA1 subfield). It was coupled with a model of the Electrode-Tissue Interface (ETI) that accounts for the biophysical properties of the intracortical microelectrode. This hybrid model was used to analyze the microelectrode geometrical (diameter, position, and direction) and physical (materials, coating) characteristics and their impact on recorded FRs. For model validation, experimental signals (local field potentials, LFPs) were recorded from CA1 using different electrode materials: stainless steel (SS), gold (Au) and Au coated with poly(3,4-ethylene dioxythiophene) /Poly(styrene sulfonate) (Au:PEDOT/PSS). *Results*: results indicated that a radius between 65 and 120 μm for a wire microelectrode is the most optimal for recording FRs. In addition, *in silico* and *in vivo* quantified results showed a possible improvement in FRs observability using PEDOT/PSS coated microelectrodes. *Conclusion*: the optimization of the design of microelectrodes for FRs recording can improve the observability and detectability of FRs which are a recognized marker of epileptogenicity. *Significance*: This model-based approach can assist in the design of hybrid electrodes (micro, macro) that can be used in the presurgical evaluation of epileptic patients with drug-resistant epilepsy.**

***Index Terms*—Electrode-electrolyte interface, epilepsy, high frequency oscillations, fast ripples, microelectrodes, polymer coating, neural recording.**

I. INTRODUCTION

Epilepsy is one of the most common neurological disorders [1]. Patients with epilepsy suffer from recurrent seizures that severely affect their quality of life [1]. In 30% of cases, epilepsy syndromes are pharmaco-resistant and the only treatment option is surgical intervention [2]. However, a positive outcome of resective surgery most often depends upon presurgical investigation and characterization of the epileptogenic network and seizure onset zone (SOZ) [2], [3]. Consequently, the demand is high for specific biomarkers that can help delineate the SOZ.

High Frequency Oscillations (HFOs; 120-600Hz), and Fast Ripples (FRs; 250-600 Hz) in particular, have been considerably studied for their potential value as biomarker of the epileptic tissue [4]–[6]. HFOs were reported to reflect the seizure severity and were found to be correlated to the seizure onset and propagation [7]. Moreover, recent studies have demonstrated that removing brain tissue generating FRs is correlated to a better surgical outcome [4], [8], [9]. However, FRs are difficult to detect in Stereo-ElectroEncephaloGraphic (SEEG) signals due to their low amplitude and high background noise [10].

Over the past two decades, microelectrodes were considerably employed for the recording of pathological FRs as they provide good selectivity and resolution [11]. However, a small dimension is associated with an increase in the electrical impedance causing high thermal noise and shunt loss [11]–[15]. This leads to the recording of distorted signals and low Signal to Noise Ratio (SNR) [16].

Recently, different high-performance microelectrodes have been designed to optimize neural recording while maintaining a high resolution and stability. Innovative approaches in fabrication techniques use a coating to increase the effective recording surface area while maintaining the electrode geometrical surface [15], [17]–[21]. The most notable coatings are Titanium Nitride (TiN), Iridium Oxide (IrOx), and conductive polymers. In particular, Poly(3,4-ethylene dioxythiophene) (PEDOT)- based coatings have emerged as one of the best materials for the neural interface due to their high biocompatibility, stability, and porous surface that significantly decreases the impedance [22], [23]. Nevertheless, the stability is extremely dependent on the dopent being used [17]. A large pallet of dopants (counter ions) have been evaluated such as tetrafluoroborate (TFB), perchlorate (ClO4-), lithium perchlorate ($LiClO_4$), phosphate-buffered Saline (PBS) and carbon nanotubes (CNT) [17], [20], [22], [23]. The most common and promising dopant used with PEDOT, though, is

---

This work was funded by the French research agency (01/10/2019, 30/09/2020, N° ANR-18-CE19-0013-01).

M. Al Harrach, G. Dauly, G. Dieuset, P. Benquet and F. Wendling are with the University of Rennes 1, Inserm, LTSI-U1099, 35000 Rennes, France (e-mail: mariam.al-harrach@inserm.fr, gautier.dauly@univ-rennes1.fr, gabriel.dieuset@univ-rennes1.fr, pbenquet@univ-rennes1.fr, fabrice.wendling@univ-rennes1.fr)

Hajar Seyedeh-Mousavi and Esma Ismailova are with Ecole Nationale Supérieure des Mines de Saint Etienne, CMP-EMSE, MOC, 13541 Gardanne, France. (e-mail: seyedeh.mousavi@emse.fr, ismailova@emse.fr).

the polystyrene sulfonate (PSS) [19].

In addition to coating features, the electrode characteristics can also impact the observability of the FRs and, thus, their detectability. These characteristics include both the geometrical features (recording surface, insertion angle, positioning with respect to the pathological tissue) and the Electrode-Tissue Interface (ETI) which is mainly related to the type of material.

So far, there are very few studies that explore the effect of the microelectrode features on the recording quality of FRs. In this work, we propose to investigate and analyze the different microelectrode parameters that directly impact the FRs detectability (amplitude, noise level…). Our approach makes use of a realistic CA1 hippocampal network model combined with an ETI model for investigating the impact of various electrode types and geometrical characteristics on simulated signals (local field potentials - LFPs). The primary objective of this study is to propose recommendations for the design of microelectrode optimized for improved recording of FRs.

II. MATERIALS AND METHODS

A. Experimental protocol and Electrode modeling

1) Electrodes preparation: Gold (Au) and Stainless Steel (SS) electrodes with 125 µm diameter were purchased from Goodfellow company (Figure 1.A). A portion of Au electrodes were coated with PEDOT:PSS following a potentiostatic electropolymerization technique in an aqueous solution of 0.01 M 3,4-ethylene dioxythiophene (EDOT) and 0.1 M Sodium Polystyrene Sulfonate (NaPSS) [24]. The polymerization potential was set at 1.1 V versus the reference electrode for a duration of 50 s. The EDOT and NaPSS were purchased from Sigma-Aldrich and used as received.

2) Electrodes characterization: Impedance spectroscopy measurements were performed in a three-electrode cell set-up in phosphate-buffered saline (PBS) solution using a Metrohm Autolab potentiostat. A platinum wire and an Ag/AgCl electrode were used as counter and reference electrodes respectively. The impedance of SS and Au electrodes with and without PEDOT/PSS was measured under an alternative voltage of amplitude equal to 0.01 V and frequency (sinusoidal wave) ranging from 10 kHz down to 1 Hz. The impedance measurements showed a significant decrease in impedance values after coating for the Au electrodes (the impedance at 1kHz decreased from 254 ± 10 k to 2.64 ± 0.5 k). Furthermore, the cut-off frequency at which the electrode transitions from predominantly resistant to capacitive was pushed down to 160 Hz [25]. The morphology of electrodes was imaged by scanning electron microscope (SEM) as depicted in Figure 1.A. Images were obtained using a Carl Zeiss Ultra55 with a secondary electron detector (SE) at 5 kV. The SEM images of coated electrodes showed a homogeneous coating of PEDOT/PSS. The PEDOT coating's stability was assessed using Cyclic Voltammetry (CV) evaluations in the same electrochemical cell. 400 CV scans were performed on gold wire coated with PEDOT:PSS between -0.9V to 0.5V with 100 mV/s scan rate [24]. Impedance spectroscopy of PEDOT:PSS coated electrodes after 400 CV scans remained the same.

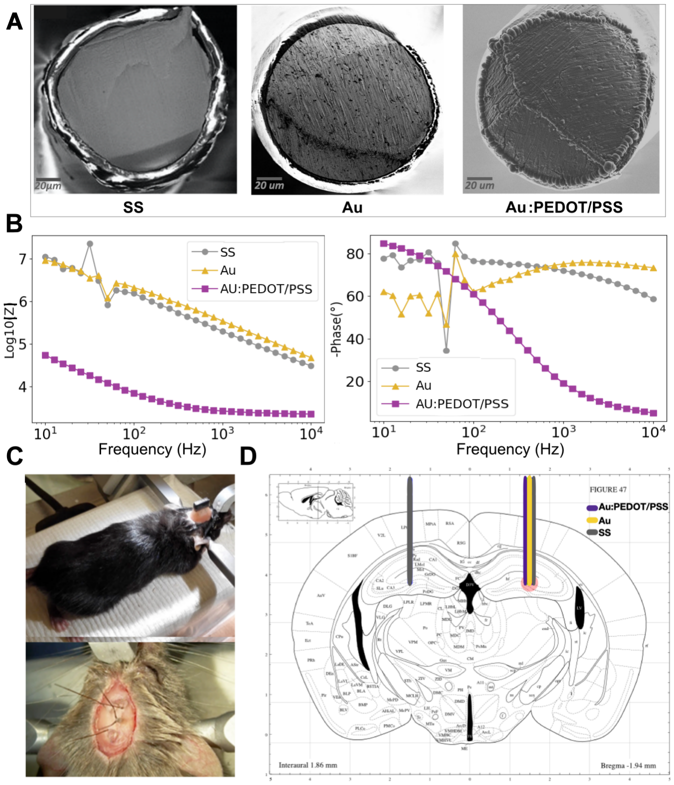

Fig. 1. Experimental protocol overview (A) SEM images of Stainless Steel (SS), gold (Au), and Au coated with PEDOT:PSS (Au:PEDOT/PSS) wire microelectrodes. All electrodes have the same diameter of 125 μm.(B) Example of Bode plots of the experimentally measured impedances via EIS for SS, Au and Au:PEDOT/PSS electrodes. (C) An image of the operating field during electrode implantation for one of the mice. The mouse is fixed in a stereotaxic frame (up). A three electrodes bundle (SS, Au, and Au:PEDOT/PSS) is inserted into the left hippocampus and one SS electrode was inserted into the right hippocampus. The reference electrode was implanted just above the cerebellum (bottom).(D) Schematic diagram of the multisite intracortical electrode implantation positions adapted from the Mouse Brain in Stereotaxic Coordinates by Paxinos and Franklin [26].

3) Surgery and EEG recording: The experimental protocol was implemented according to the Kainate mouse model of epilepsy [27]. This experiment respected the European Communities Council Directive of 24 November 1986 (86/609/EEC) and was approved by the ethics committee on animal experimentation in Rennes, France (agreement N° APAFIS # 2327-2015101914507202). Four 80 weeks-old C57BL/6J male mice were used in the experimental protocol. During the surgery, the mice were anesthetized and placed in a stereotaxic frame. Then, they were injected with a dose of 50 nl of a 20 mM solution of kainic acid (KA; Sigma-Aldrich) in 0.9% NaCl. The injection was unilaterally localized in the right dorsal hippocampus (Figure 1.B and C).

All mice were implanted with three depth electrodes (SS, Au, and Au coated with PEDOT/PSS) in the left hippocampus. In addition, one SS electrode was placed in the right hippocampus (CA1 region, Figure 1.C). The reference electrode was implanted above the cerebellum. After implantation, the five electrode wires were first welded into the connector attached to the acquisition system. Then, the connector was fixed on the skull of the mouse via dental acrylic cement

This article has been accepted for publication in IEEE Transactions on Biomedical Engineering. This is the author's version which has not been fully edited and content may change prior to final publication. Citation information: DOI 10.1109/TBME.2023.3250763

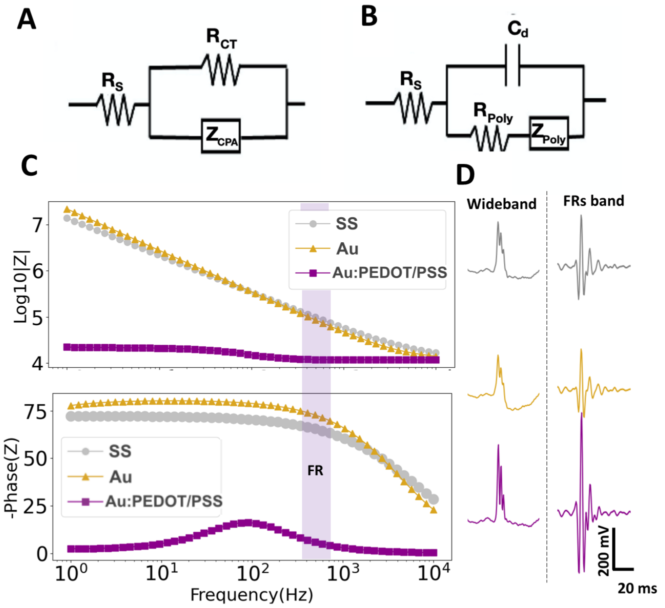

Fig. 2. Equivalent circuit models characteristics. (A) The circuit elements of the metal microelectrodes (stainless steel (SS) and Gold (Au)) consisted of the spreading resistance ($\boldsymbol{R_s}$), the charge transfer resistance ($\boldsymbol{R_{CT}}$), and the constant phase angle impedance ($\boldsymbol{Z_{CPA}}$). (B) The equivalent circuit elements of the PEDOT/PSS coated Au electrodes (Au:PEDOT/PSS) are the coating capacitance ($\boldsymbol{C_d}$), Charge transfer polymer resistance ($\boldsymbol{R_{CT_{Poly}}}$), and double layer interface impedance ($\boldsymbol{Z_{Poly}}$). (C) Bode diagram for the three electrode types (SS, Au, and Au/PEDOT/PSS). These frequency responses are simulated for 125 $\boldsymbol{\mu m}$ diameter electrodes placed in the mice brain. The values of the equivalent circuit parameters are depicted in Table 1. (D) An example of a Fast Ripple (FR) segment recorded with each electrode type obtained in vivo from Mouse S1.

(Figure 1.B). The different positions of electrodes implantation and KA injection (coordinates from bregma) were as follows:

- KA injection: AP=-2.0 mm, ML=-1.5 mm, DV=-2 mm
- LH Electrode Bundle: AP=-2.0 mm, ML=-1.5 mm, DV=-2 mm
- RH Electrode: AP=-2.0 mm, ML=+1.5 mm, DV=-2 mm

The intracortical electrode placements were chosen using the mouse brain atlas [28]. The three wires of 125 µm diameter isolated by polyester (SS, Au, and Au:PEDOT/PSS) were attached together to create a bundle that was inserted at once. After the surgery, animals were left in their cage to recover for three days in preparation for the recording sessions. LFP signals were recorded for 2 hours using an EEG monitoring system (Deltamed TM) and were sampled at 2048 Hz. During the recording sessions, each mouse was freely moving in a transparent Plexiglas cage, itself placed in a Faraday cage. Recordings were performed once a week for four weeks. For the purpose of this study, only the first week recordings were exploited. In addition, after visual inspection and analysis of the post-recording signals, three of the four mice were found to be epileptic. Therefore, the non-epileptic mouse was excluded from further processing.

4) Electrode Tissue Interfaces : Two different equivalent circuits were used to model the ETI; a general one for commonly used metal electrodes and a modified version for PEDOT/PSS- coated electrodes (Figure 2.A, B). They were chosen to best fit the actually measured impedance. The first is adapted from Randle's model frequently used to describe the electrode interface impedance [29], [30]. It consists of a spreading resistance R_S in series with the double layer elements including a capacitive element Z_{CPA} in parallel with a charge transfer resistance R_{CT} (Figure 2.A). The spreading resistance, also called electrolyte resistance, R_S represents the impedance between the working and the counter electrode and is obtained by [21]:

$$R_S = \frac{\sigma\sqrt{\pi}}{4\sqrt{A_e}} \tag{1}$$

With σ the solution resistivity and A_e the electrode's geometrical surface. For a circular electrode of radius r, (1) is expressed as $R_S = \frac{\sigma}{4r}$. The charge transfer resistance R_{CT} is the faradaic impedance that describes the charge leakage across the double layer and is expressed by [21]:

$$R_{CT} = \frac{RT}{zFi_0} \tag{2}$$

Where R and F are the gas and faraday constants respectively, T is the temperature in K, i_0 is the current density.

The non-faradaic element of the double layer, which accounts for its charging, is the constant phase angle impedance Z_{CPA}. Formerly, this element was expressed as a simple capacitance (C_{dl}) introduced by Stern after combining both the Helmholtz double layer capacitance C_H and the Gouy-Chapman diffuse layer capacitance C_D [21] as presented below:

$$\frac{1}{C_{dl}} = \frac{1}{C_D} + \frac{1}{C_H} = \frac{d}{\epsilon_0\epsilon_r} + \frac{\sqrt{\frac{\epsilon_0\epsilon_r U_t}{2n^0 z^2 q}}}{\epsilon_0\epsilon_r cosh(\frac{z\phi_0}{2U_t})} \tag{3}$$

With ϵ_0 and ϵ_r the permittivity of free space and double layer respectively, z the ion charge in the solution, U_t the thermal voltage, ϕ_0 the electrode potential, q the elementary charge, and $n0$ the ion concentration bulk number.

Later on, it was found that this impedance is not purely capacitive due to the inhomogeneous electrode surface [21]. Accordingly, it is expressed by the pseudocapacitance empirical equation in (4).

$$Z_{CPA}(\omega) = \frac{1}{C_{dl} j\omega^n} \tag{4}$$

Where n is a constant between 0 and 1 and ω is the angular frequency. We have to note that the Warburg impedance was excluded from this ETI model since its irrelevance in the frequency band of interest to this study [21].

The second model is elaborated to characterize the impedance response of the PEDOT/PSS- coated electrodes. Ideally, the impedance response of an organic coating is equivalent to its dielectric capacitor and is obtained by equation (5). However, in such systems a defect-free coating is impossible. Therefore, in parallel with the coating (dielectric) capacitance, new double-layer elements were added. These elements consisted of a charge transfer resistance relative to

This article has been accepted for publication in IEEE Transactions on Biomedical Engineering. This is the author's version which has not been fully edited and content may change prior to final publication. Citation information: DOI 10.1109/TBME.2023.3250763

the polymer $R_{CT_{poly}}$ in series with a constant phase element (Z_{poly}) describing diffusion due to the porous surface of the polymer [20]–[22].

$$Z_C = \frac{-j}{C_d\omega}, C_d = \frac{\epsilon\epsilon_0 A}{d} \tag{5}$$

Where ϵ_0 and ϵ are the dielectric constants of free space ($8.85 \times 10^{-14} F/cm$) and coating material respectively, A is the surface area and d is the coating thickness. It is noteworthy that apart from the R_S which depends on the geometrical surface (equation (1)), all circuit element values depend on the effective surface area of the electrode [21].

The circuit elements defined above were used to compute the transfer function (H(f)) of the recording electrode that will, later on, be used to simulate the recorded LFP signal. This allows us to incorporate the biophysical characteristics of the electrode in the simulation of the signals. The types of circuit elements and their respective values have a direct impact on the transfer function H(f) of the ETI. The transfer functions for each of the circuits are depicted in Appendix II (Please refer to equations (10), (11), and (12)).

The values of the equivalent circuit elements for each of the three electrodes used in this study were obtained by fitting the EIS impedance measurements using EC-LAB Software 11.3. The mean values from different fitting measurements were then employed in the ETI model. The values are presented in Table I. These electrodes were compared to Platinum (Pt), Pt Black, and TiN electrodes that are commonly used in other studies. The two chosen circuits presented very good fitting results with the measured data using the Randomize + Simplex fitting algorithm provided by the EC-LAB software as depicted in Table II. In addition, The PEDOT/PSS- coated electrode was also compared to other conducting polymer coating procedures that include different counterions than the PSS. These microelectrodes are PEDOT/CNT [16], PEDOT/$LiClO_4$ [20] and PEDOT/TFB [22]. The equivalent circuit values of these electrodes are listed in the Appendix.

TABLE I

THE DIFFERENT VALUES OF THE EQUIVALENT CIRCUIT ELEMENTS USED IN THE ETI MODEL FOR THE STAINLESS STEEL (SS), GOLD (AU), AND PEDOT/PSS COATED GOLD (AU:PEDOT/PSS) ELECTRODES

Circuit Elements	**SS**	**Au**	**Au:** PEDOT/PSS
$R_S(\Omega)$	1,244 $\times 10^3$	3,748 $\times 10^3$	2,339 $\times 10^3$
$R_{CT}(\Omega.um^2)$	7,286 $\times 10^{12}$	1,412 $\times 10^{11}$	—-
$C_{dl}(F.um^2)$	1,387 $\times 10^{-13}$	7,141 $\times 10^{-15}$	—-
$R_{CT_{Poly}}(\Omega.um^2)$	—-	—-	$9,107 \times 10^7$
$C_{dl_{poly}}(F/um^2)$	—-	—-	5,204$\times 10^{-12}$
$C_d(F.um^2)$	—-	—-	1,404 $\times 10^{-11}$
n	0,9268	0,8803	0,9458
χ^2	9.049 $\times 10^{-1}$	3.329 $\times 10^{-2}$	4.154 $\times 10^{-2}$

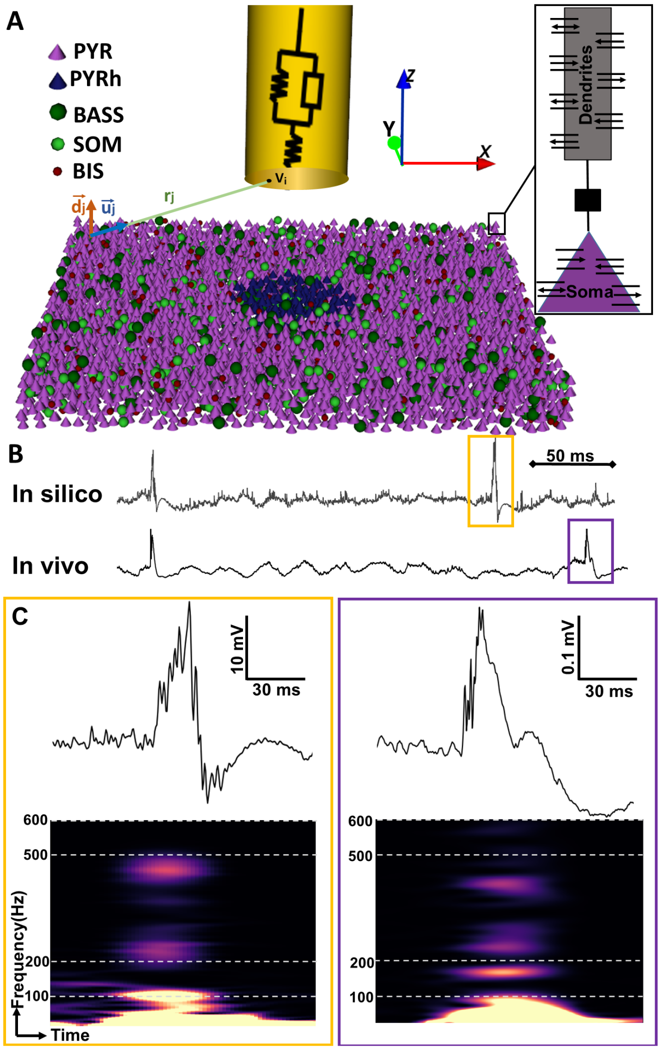

Fig. 3. Epileptic neural network structure and comparison between real and simulated local field potentials (LFPs) with Fast Ripples (FRs). (A) An example of the CA1 subfield (hippocampus) neural network structure including Pyramidal ($\boldsymbol{PYR}$) and hyperexcitable PYR ($\boldsymbol{PYR_h}$)cells (6991) in addition to Basket (BAS, 477), Oriens-Lacunosem Moleculare (OLM, 477), and Bistratified (BIS, 477) interneurons. Each PYR cell is represented by a two-compartment model (please refer to [31] for a detailed description). (B) An example of a two-second long extracellular field potential obtained *in silico* and *in vivo*. The real signal was recorded with intracerebral depth electrodes (125 $\boldsymbol{\mu m}$ diameters) from a mouse hippocampus treated with kainic acid (kainate model of temporal lobe epilepsy). The *in silico* signal was obtained by simulating an electrode with the same characteristics as the one used in vivo. (C) A zoom-in representation of the real and simulated LFPs with superimposed FRs (up) along with corresponding spectrograms (bottom) that highlight the presence of signal energy in the FRs frequency band (250-500 Hz).

B. Computational Model

1) Neural Network: A 3D neural network model mimicking the CA1 subfield of the hippocampus was used for the simulation of physiologically-relevant interictal HFOs as observed in LFPs. This physiologically and biophysically neuroinspired computational model was adapted from Demont-Guignard et al. [31], [32]. In brief, it consists of a detailed network of principal neurons (pyramidal (PYR)) cells and three different types of interneurons: basket cells (BAS) that target the PYR cell somata and oriens-lacunosum moleculare (OLM) and bistratified (BIS) cells that target PYR cell dendrites (Figure 3.A). These cells were synaptically interconnected by respecting the known features of the hippocampus circuitry [33]. Reduced two-compartments and single-compartment models were used for the excitatory PYR cells and the inhibitory

This article has been accepted for publication in IEEE Transactions on Biomedical Engineering. This is the author's version which has not been fully edited and content may change prior to final publication. Citation information: DOI 10.1109/TBME.2023.3250763

interneurons, respectively. Various somatic and dendritic ion currents were incorporated in these compartments as they play a potential role in epilepsy, [31]. Cell membrane properties were expressed using the Hodgkin-Huxley formalism. For a more in-depth description of the original model please refer to [31].

Simulations consisted of a $600 \times 600 \times 50 \mu m^3$ volume describing a realistic 3D element of the CA1 subfield. It included a total number of 7163 cells (5731 neurons and 1432 interneurons). The number of neurons was obtained from a 0.3184 million/mm3 density computed from the CA1 area and PYR total number values as previously published [34], [35]. The 1432 interneurons corresponding to 20% of the total cell number were equally divided between the three subtypes (BAS, OLM, and BIS) resulting in 477 interneurons per subtype. Mitchel's best candidate algorithm was used for the spatial placement of the neural network cells [36]. An example of the neural network structure is depicted in Figure 3.A. Along with the CA1 network, an additional network of 1260 neurons was simulated to mimic the CA3 input to CA1 via the Schaffer collaterals. These cells were placed outside the network and were connected through glutamatergic synapses. Overall, simulated inputs targeted both glutamatergic ($AMPA_R$ and $NMDA_R$) and GABAergic synapses ($GABA_R$).

In order to reproduce realistic FRs, we adjusted the properties of a small number of PYR cells to create hyperexcitable neurons that contribute to an epileptic neural network [37]. This was done by selecting a cluster of neurons inside a 80 μm radius sphere at the middle of the whole neural network (Figure 3.A) and increasing their GABA reversal potential (from E_{GABA} = -75 mV to -50 mV). The size of the cluster was chosen based on [37]. It allows us to simulate realistic FRs as the ones recorded in early epileptogenesis.

The simulation of intracellular membrane potentials in CA1 was done using a stimulation input signal that targeted the CA3 PYR cells which in turn stimulated the CA1 neural network. This input signal comprised: 1) multiple randomized occurrences of uniformly distributed volleys of action potential with uniform jitters that mimic CA3 input resulting in background activity or theta rhythm. 2) One volley of action potentials gaussianly distributed around a fixed value determined by a beta law and a small jitter resulting in highly synchronized evoked action potentials that can simulate transient events with a frequency of $0.4Hz$ [38]. Lastly, the simulated LFP recorded by the electrode is obtained as follows: First, the net potential V observed at the electrode was approximated as the algebraic mean of the closely discretized extracellular points potentials v_i over the electrode surface [39]. Subsequently, each PYR cell j is considered as a current dipole source, and the potential v_i at a point i is computed as the sum of the contribution of all PYR cells (Please refer to Figure 3.A). The extracellular point potentials v_i are obtained using the dipole theory, as depicted in (6), wherein only PYR cells contribution is considered [31].

$$v_i = \sum_{j=1}^{n} \frac{\vec{d_j}.\vec{u_j}}{4\pi.\sigma.{r_j}^2} \qquad (6)$$

Where $\vec{d_j}$ is the dipole moment, $\vec{u_j}$ and r_i are the unitary vector and the distance between the recording point i and PYR cell j respectively, σ is the conductivity of the brain volume assumed to be homogeneous in this study. Then, the LFP signal recorded by the microelectrode is computed by applying the inverse Fourier transform to the product of the ETI transfer function $H(f)$ and the extracellular potential $V(f)$ in the frequency domain.

To test the impact of the electrode materials on the recorded signal, we simulated 3 configurations x 300 stimulation profiles = 900 signals. In addition, 300 signals with large CA1 volume were simulated in order to test the impact of the electrode geometrical parameters by taking into account the electrode recording range. The model simulation parameters were adapted based on the work of Al Harrach et al. [37] to portray the seventh day of the epileptogenesis for three different model configurations (randomized cell positions based on the best candidate's algorithm). This allowed us to propose an optimal electrode design. The Model was developed using Python 3.7 on Pycharm IDE. The simulations were performed on an Intel(R) Xeon(R) Gold 5220R@ 2.20GHz CPU Computer with 192-GB memory.

C. Signal processing and FR characterization

1) FR segmentation: For the experimental signals, the delineation of FRs was done manually on the wideband filtered LFPs. Segments of 0.5 ms were chosen after convolution with Gabor wavelets in the FR band (200-600 Hz) if they complied with the following criteria: a) they contain at least four clear oscillations b) their amplitude is at least twice the amplitude of the background. c) they are easily spotted in the signal spectrogram and are not a harmonic of a lower frequency oscillation.

For both experimental and simulated signals, the same segmentation pipeline was applied. This pipeline is based on the Watershed image segmentation algorithm previously published in [37]. It consists of automatically extracting the boundaries $t0$ (start) and $t1$ (end) of each FR by segmenting the corresponding spectrogram image in the FR band [37] as shown in Figure 4.C. An example of the segmentation result for a simulated and a recorded signal is depicted in Figure 4.A and 4.B respectively.

2) Feature selection and statistical analysis: In order to characterize the FR observability, two metrics were used: The FR Index and the RMS. The FR_{index} represents the ratio between the power of the FR oscillation and the total power of the signal in the FR segment. It is obtained using (7).

$$FR_{index} = \frac{\sum_{i=t_0}^{t_1} x_{200-600}([i])^2}{\sum_{n=t_0}^{t_1} x_{3.5-200}([i])^2} \qquad (7)$$

Where $x_{200-600}$ is the segmented FR, $x_{3.5-600}$ is the corresponding background and t_0 and t_1 are the first and last samples of the FR segment respectively. In the case of simulated signals, the FR attenuation due to the recording electrode material was computed using the attenuation ratio

This article has been accepted for publication in IEEE Transactions on Biomedical Engineering. This is the author's version which has not been fully edited and content may change prior to final publication. Citation information: DOI 10.1109/TBME.2023.3250763

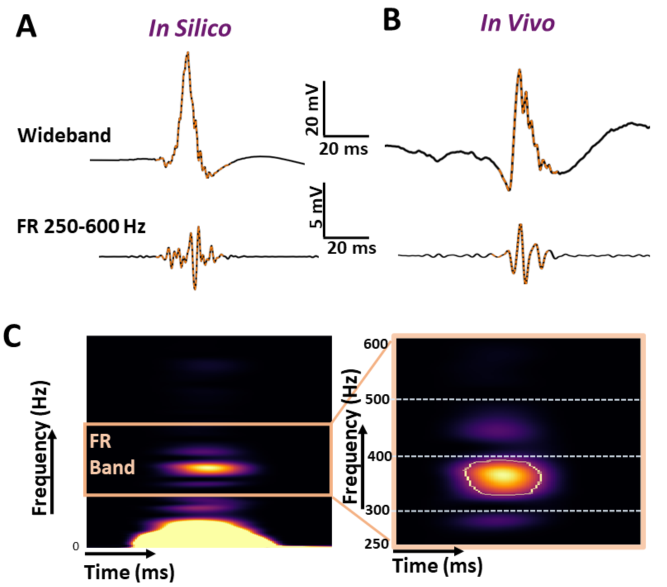

Fig. 4. An example of a real versus a simulated Local Field Potential (LFP) with FRs. The segmented FR is depicted in orange in the wideband signal (top) and the FR band-filtered signal (bottom). (A) The FRs segment delineation in the simulated signal. (B) The FRs segment delineation in the experimental signal. (C) An example of the segmentation pipeline applied on the spectrogram of the simulated signal in (A). The watershed-based algorithm outlines the start and finish of the FRs

depicted below [40]:

$$\Delta FR(\%) = \frac{FR_0 - FR_m}{FR_0} \tag{8}$$

Where FR_0 and FR_m are the FR energies before and after adding the ETI corresponding to a material type m. We also computed the thermal noise for each electrode using the Johnson-Nyquist formula [41]:

$$Noise(\delta f) = \sqrt{4kTR_e(Z_e)\delta f} \tag{9}$$

Where k is the Boltzmann constant, T is the absolute temperature, $R_e(Z_e)$ is the real part of the electrode impedance and δf is the noise bandwidth. Thermal noise can seriously affect the quality of the recorded signal and is directly linked to the materials and radius of the electrode used.

For statistical comparison of the electrode materials in terms of FR observability, non-parametric Welch's t-test and paired t-test were performed on FR metrics for both simulated and recorded signals. FR indices and RMS values were considered as significantly different for $p < 0.01$.

III. RESULTS

A. Microelectrode materials

As previously stated, the microelectrode material plays a crucial role in the recording efficacy, reliability, and lifetime [42]. In addition to the three electrode types that were fabricated (SS, Au, and Au:PEDOT/PSS), we analyzed data from other commonly used materials: Platinum (Pt), Pt Black and Titanium nitride (TiN) [21]. Figure 5.A shows the ETI transfer function modulus and noise PSD of the six electrode types mentioned above. For the SS, Au, and Au:PEDOT/PSS electrodes that were used in the experimental study, a comparable attenuation between 10 and 12 dB is observed for the Au and SS electrodes in the FR frequency band. However, for the PEDOT/PSS coated Au electrodes we observed a considerably lower impedance (Figure 2.C) and accordingly a higher transfer function modulus (Figure 5.A). This result is directly linked to the increase of the double layer capacitance as indicated in Table I. Similarly, the Pt and Pt black electrodes displayed slightly better performances than the SS and Au electrodes explained by their higher double layer capacitance values (Table II and Figure 5.A). The TiN microelectrode, on the other hand, had a comparable attenuation impact to the PEDOT/PSS-coated gold electrodes. However, they suffered from higher thermal noise PSD values as shown in Figure 5.A. Altogether, the electrodes act as a low pass filter wherein the gain and cut-off frequency is directly linked to the double layer capacitance. Moreover, in the FR Band, the lowest attenuation is provided by the Au:PEDOT/PSS electrode. The noise spectral density portrayed a $1/f$ profile at low frequencies and reached a plateau at higher frequencies for SS, Au, TiN, and Pt electrodes. The lowest thermal noise was observed for the Au:PEDOT/PSS electrodes and Pt Black electrodes with an almost constant profile variation with a frequency increase (Figure 5.A). The aforementioned thermal noise is directly linked to the charge transfer resistivity of the ETI that represents the faradaic reactions happening during the recording of LFPs. As described by equation (9), the thermal noise is higher for higher charge transfer values, particularly for lower frequencies ($< 1KHz$) The impedance modulus and phase for the PEDOT doped with PSS microelectrodes compared to other PEDOT electrodes with three different counterions (TFB, CNT and Li, ClO_4) are depicted in Figure (5.B). In the FR frequency band (250-600 Hz) all the PEDOT-coated electrodes have similar impedance characteristics with primarily resistive behavior as opposed to the capacitive behavior of the Au and SS electrodes (Figure 2.C). In contrast, for low frequencies, we observed a much higher impedance (more than one order of magnitude) for the PEDOT/$LiClO_4$ compared to the others (figure 5.B). The lowest impedance was obtained for the PEDOT/PSS electrode. Moreover, the PEDOT/PSS showed a predominately resistive behavior, independently from the frequency, compared to the capacitive profile of the PEDOT/TFB and PEDOT/CNT electrodes at low frequencies. For the SS, Au, and Au:PEDOT/PSS microelectrodes used in this study we computed the FR_{Index} and ΔFR of their corresponding simulated signals ($900 signals \times 3 types$). The results are presented in figure 5.C. Significant improvements were noticed in FR observability for PEDOT/PSS coated microelectrodes compared to the SS and Au microelectrodes. The FR_{Index} is 88% higher for the PEDOT/PSS and the FR attenuation was only about 2% compared to 69% and 76% for the Au and SS microelectrodes respectively. Moreover, the Au:PEDOT/PSS preserved the lower frequency contents of the recorded signals as shown by the simulated LFP segments in 5.C.

This article has been accepted for publication in IEEE Transactions on Biomedical Engineering. This is the author's version which has not been fully edited and content may change prior to final publication. Citation information: DOI 10.1109/TBME.2023.3250763

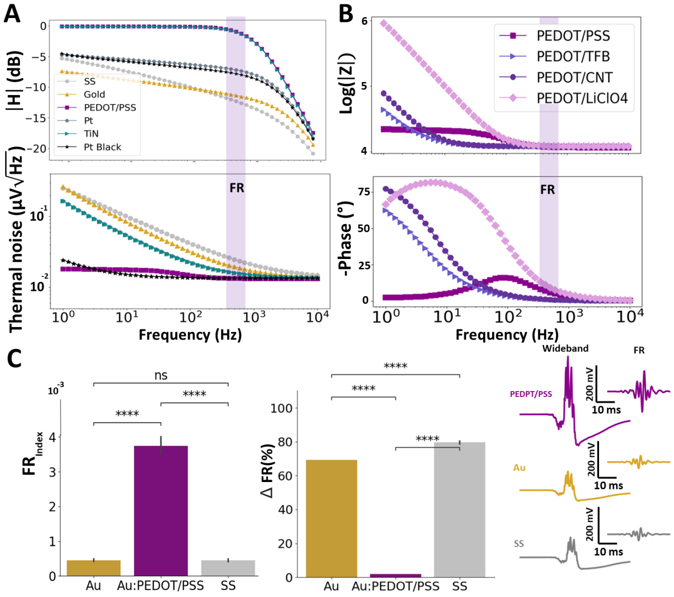

Fig. 5. Impact of the electrode materials on the FR observability. (A) ETI transfer function (H) and noise power spectral density (PSD) variation with frequency simulated for the different types of electrodes (SS, Au, Au:PEDOT/PSS, Pt, Pt black and TiN) of 125 $\boldsymbol{\mu m}$ diameter.(B) Bode plot of the electrode impedance for different types of counterions coating with PEDOT (PSS, TFB, CNT and $\boldsymbol{LiClO_4}$). (C) Comparison of the $\boldsymbol{FR_{Index}}$ (left) and the $\boldsymbol{\Delta FR}$ (middle) for the three types used in the experimental recordings (SS, Au, and Au:PEDOT/PSS) with an example of simulated signals recorded for each type (right).

B. Geometrical Characteristics of the microelectrode

Electrode size, positioning, and orientation also intervene in the amplitude and shape of the activity recorded by the electrode. The larger the electrode the larger the recording field over a given area. However, higher radius results in higher spatial averaging resulting in a blurring effect on local events and loss of spatial selectivity. Furthermore, the position and orientation of the electrode with respect to the area of interest can also notably affect the recorded activity. In this section, we report simulation performed to study the impact of the electrode size, position and insertion angle on the shape of the recorded FRs.

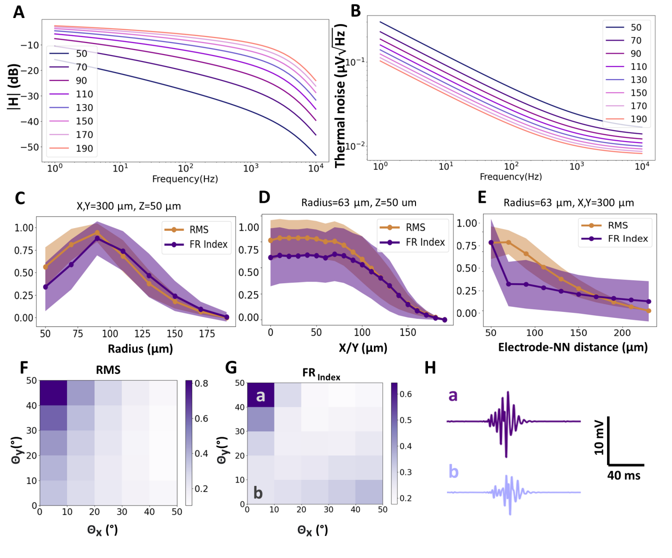

Fig. 6. Impact of the microelectrode geometrical characteristics on the FR observability in the case of a SS electrode of $\mathbf{125\mu m}$ diameter. (A) Variation of the H modulus with frequency for different electrode radii. (B) Variation of the thermal noise spectral density with frequency variation for different radii. (C),(D) and (E) Impact of the microelectrode radius, X/Y position, and depth (Z), respectively, on the normalized FR Index and FR RMS. Influence of the electrode insertion angle on the FR RMS (F) and FR Index (G). (H) an example of FR signal (250-500 Hz) for two different insertion angles

1) Impact of the electrode size: The electrode size plays a major role not only in the spatial averaging but also in the modification of the ETI element values and thence its impedance. Figures 6.A presents the impact of the electrode radius on the transfer function (TF) profile. As expected, the TF modulus increases with the radius. This increase is more pronounced at higher frequencies. In the FR band and for SS electrodes, the mean attenuation due to the ETI is equal to -33 dB for a 50 μm radius compared to -7 dB for a 190 μm radius (Figure 6.A). Inversely, the thermal noise spectral density decreases with the electrode effective surface as demonstrated in Figure 6.B. The global impact of the radius (spatial averaging + impedance) is portrayed in Figure 6.C. Both RMS and FR_{Index} values decrease with electrode size starting from 80 μm radius suggesting that the optimal electrode radius is between 65 and 125 μm.

2) Position and insertion angle: Figures 6.D and E show the variation of the FR features with the electrode X/Y position and distance (Z) with respect to the center of the simulated CA1 tissue respectively (Figure 3.A). Both FR RMS and FR_{Index} decrease as the electrode distance from the cluster of neurons increases (depth and X/Y placement). Regarding the electrode angle, results suggest that it also plays a role in FRs observability. The highest FR RMS and Index values were found for $= 0$ and $= 50$ (Figures 6.F, D, and H).

C. Experimental validation

A total of 1200 FR segments for each electrode type (SS, Au, and Au:PEDOT/PSS) were obtained from the signals recorded in three mice. The quantitative comparison of recorded FRs is provided in Figures 7 for day 7 after kainate injection. The FR_{Index} and FR RMS were found to be significantly higher for Au:PEDOT/PSS than SS and Au microelectrodes in the case of mice S1 and S4 in accordance with the simulation prediction. The mean FR_{Index} values were about three and four times higher for the Au:PEDOT/PSS microelectrodes compared to the Au and SS electrodes for S1 and S4 respectively. Furthermore, SS microelectrodes had significantly higher FR_{Index} values than Au. The mean FR_{Index} value for the SS was about 28% and 34% higher than that of the Au microelectrode in the case of S1 and S3 respectively. For S3, and as discussed hereafter, it is worth noting that higher RMS values were found for the Au microelectrode and the lowest for the PEDOT-coated one.

IV. DISCUSSION

The recording of FRs is recognized to be very valuable in the context of refractory epilepsy where depth electrodes are

This article has been accepted for publication in IEEE Transactions on Biomedical Engineering. This is the author's version which has not been fully edited and content may change prior to final publication. Citation information: DOI 10.1109/TBME.2023.3250763

being used during pre-surgical evaluation. Considering that FRs can help delineate the SOZ [2], [3], a perspective is to use the detection FRs as complementary information to define the resection strategy. In this study, we investigated model-guided understanding of microelectrodes characteristics for optimized recording and detection of FRs. Using a physiologically-relevant computational model of a 3D cortical volume combined with a biophysical model of ETI, very realistic interictal FRs were simulated (Figures 3 and 4). This in silico approach allowed us to analyze the capacity of LFPs to reveal FRs which is a crucial factor for automatic detection. These parameters are divided into geometrical characteristics comprising of the electrode's effective surface, position, and direction, on one hand, and physical characteristics that are defined by the electrode material on the other hand.

Comparisons between six types of electrode materials, with the same surface area, SS, Au, Au: PEDOT/PSS, Pt, Pt Black, and TiN revealed that Au:PEDOT/PSS electrodes lead to minimal distortion of recorded signals. Particularly, in the FR band, it has the lowest attenuation due to the transfer function. This is explained by the decrease in impedance between Au and PEDOT/PSS- coated microelectrodes and is portrayed by the higher double layer capacitance value (Table I). This is explained by the fact that coated electrodes have the highest double layer capacitance induced by their higher effective area [19]. Furthermore, Au:PEDOT/PSS electrodes produce the minimum thermal noise (Figure 5.A) in the bandwidth $0 - 1KHz$ wherein thermal noise has a major impact on the signal to noise ratio of the recorded signal [43].

Another advantage of PEDOT-coated electrodes is their flexibility which promotes better cell attachment and less glial tissue formation around the microelectrode [23]. Moreover, PEDOT was found to be the most stable conductive polymer for implantable devices wherein the dopant/counterion plays an important role [17]. Accordingly, PSS was compared to three other dopants used with PEDOT for neural recording/stimulation (Figure 5.B). The impedance Bode plots for the coated electrodes were similar in the FR band. Nevertheless, in the high gamma and ripple frequency band (80-250 Hz) the $PEDOT/PSS$ had slightly higher impedance modulus than the $PEDOT/TFB$ and $PEDOT/CNT$ ones and the $PEDOT/LiClO_4$ revealed to be the less favorable (Figure 5.B). In the work of Kozai et al. [17], PSS was compared to CNT where CNT dopant was found to be more stable for chronic use but both had similar performances in short-term recordings. These predictions about the PEDOT/PSS ability to improve the FR observability in the recorded signals were confirmed in silico, where the FR_{Index} was significantly superior (88%) and the FR attenuation was only about 2% (Figure 5.C).

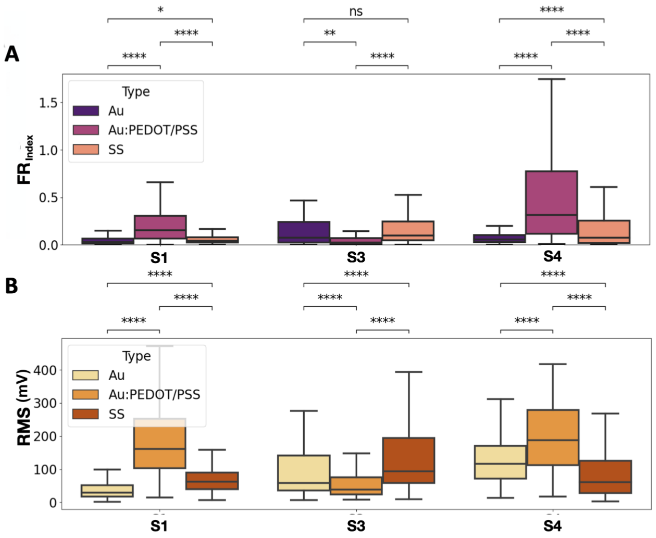

Fig. 7. Experimental results for FRs observability in three epileptic mice. Box plots of the FR_{Index} (A) and FRs RMS (B) values for SS, Au, and Au:PEDOT/PSS microelectrodes relative to mice S1, S3, and S4. Statistical analysis are represented as follows: Non Significant (ns) : $5^{-2} < p <= 1 * : 10^{-2} < p <= 5.10^{-2} * * : 10^{-3} < p <= 10^{-2} * ** : 10^{-4} < p <= 10^{-3} * * * * : p <= 10^{-4}$

Using the computational model, we investigated the impact of the electrode surface size on the recorded FRs. The 3D volume used for the simulation of the local field potential was adequately chosen $(600 \times 600 \times 50um^3)$ to take into account the electrode recording range with increasing disc radius. We could verify that the electrode impedance increases with decreasing radius (real and effective surface in general) causing higher thermal noise and attenuation (see Figure 6.A and 6.B). At the same time, the microelectrode geometrical surface (disc in the case of this study representing the tip of the wire electrode) induces a spatial averaging of activities arising from the cluster of hyperexcitable neurons that generate the FRs that is portrayed by a blurring effect of local events. In the case of FRs, their observability depends not only on the radius of the electrode but also on the locations of neuronal dipole sources. The profile variation of the FR_{Index} and RMS depicted in 6.C shows a decrease in the observability of FRs beginning around 80 μm which is in the range of the hyperexcitable cluster radius. For an electrode radius with a range smaller than the hyperexcitable cluster, we fail to record all the sources for the FRs that results in a lower FR_{Index} and RMS as depicted in Figure 6.C. Our modeling results suggest that the ideal radius that offers a good tradeoff between impedance and surface area is between 65 and 120 μm. These results are further validated by the experimental signals recorded with electrodes of 125 μm diameter and exhibiting FRs.

Along the same line, the position of the electrode (X/Y) and distance with respect to the neural network remarkably impact the recording of FRs as depicted in 6.D and E respectively. For the translation of the electrode along the X/Y axes as long as the firing neurons are in the electrode scope $(X/Y < 100)$ recorded FRs are not modified. Similarly, for the depth of the microelectrode, the amount of FRs decreases with the distance from the cluster of hyperexcitable neurons. The last tested geometrical parameter was the significance of the electrode insertion angle (Figure 6.F and G). Our results revealed less impact than the position of the electrode. Nonetheless, larger-amplitude FRs were recorded for small inclination of the microelectrode. This is explained by the fact that with a slight inclination in one direction, the outermost edge of the elec-

This article has been accepted for publication in IEEE Transactions on Biomedical Engineering. This is the author's version which has not been fully edited and content may change prior to final publication. Citation information: DOI 10.1109/TBME.2023.3250763

trode becomes even closer to the hyperexcitable firing neurons resulting in larger amplitude FRs. Based on these results, it seems that in addition to the recording surface size, the proximity to the hyperexcitable neurons firing asynchronously is a parameter that impacts the observability of FRs for a given electrode material. Regardless of the distance, the model shows that an insertion angle perpendicular to the surface of the brain is adequate to record good quality FRs as verified in the experimental recordings.

In the case of experimentally recorded FRs, RMS and FR_{Index} values obtained after segmentation of 1200 FRs revealed consistent results for mice S1 and S4 at day 7 (after kainic acid injection). As depicted in Figure 7, significant improvements in the observability of recorded FRs was found for PEDOT/PSS-coated microelectrodes as shown by higher RMS and FR_{Index} values. For these two mice the improvement in FR_index, which was three and four times higher for Au:PEDOT/PSS compared to the Au and SS microelectrodes, was in line with the results predicted by the computational model (Figure 5.C). However, opposite results were found for mouse S3. A decrease in the FR RMS as well as in the FR_{index} was found for Au:PEDOT/PSS compared to SS and Au microelectrodes. These results are contradictory to those predicted by the model (88% improvement). Instead, in this particular mouse, we found a 78% worsening for Au:PEDOT/PSS compared to the Au electrode. A possible explanation would be an early degradation of the PEDOT/PSS coating. We have to note that the glial encapsulation tissue was not taken into account in this study due to the fact that the three electrodes (SS, Au, and Au:PEDOT/PSS) were attached and inserted into the same position in the hippocampus. Thus, the tissue reaction is the result of all three electrodes and cannot be dissociated to portray each electrode's reaction. We should also mention that the glial encapsulation tissue is an important cause of an increase in the impedance with respect to the one measured in PBS solution [44]. Another rationale would be an early degradation due to the peeling of the PEDOT/PSS. Regarding the thermal noise which is estimated to be less for the Au:PEDOT/PSS electrode, it seems to be the case for S1 and S4. Nonetheless, the thermal noise is not the only type of noise present in these recordings as the ”biological” activity from the surrounding neurons also creates a background noise that can also be recorded depending on the microelectrode surface area [43]. Finally, this work presents a novel computational modeling approach that allows analyzing the sensitivity to various parameters that directly impact recorded local field potentials, in particular during FR events. It offers a non-invasive approach to microelectrode design and optimization to the recording of neural signals and detection of specific events.

Limitations of this study reside, first, in the experimental protocol that lacked *in vivo* impedance measurements which could give more insights about the impedance variation after implantation. Second, in one of the three epileptic mice used in this study, results did not match those obtained in the two others. Future work will include a higher number of mice and in vivo spectroscopy to analyze the impedance variation after implantation. Third, due to computation time, the model prevents us from simulating long periods of cerebral tissue activity wherein we can test the performance of automatic detection of FRs based on the use of classical and PEDOT/PSS-coated electrodes.

V. CONCLUSIONS

This work emphasizes the value of modeling approaches to analyze in depth characteristics of microelectrodes and to improve the recording of FRs recognized as a marker of epileptogenic brain regions. In silico, the analysis of geometrical parameters demonstrated the necessity of the electrode proximity to the epileptic tissue. It also highlighted the impact of the electrode size that should be considered when recording FRs. In addition, preliminary *in vivo* recordings showed improvement in the FRs observability as predicted by computational modeling, for PEDOT/PSS-coated microelectrodes for two mice out of three. Future work will include more animals to further validate the computational model predictions. We will, also, include in vivo impedance spectroscopy measurement as well as electrode track histology to complement results reported in this first neuro-inspired computational modeling approach for optimization of FRs recording and detection.

VI. APPENDIX I

TABLE II

ELECTRODE TISSUE INTERFACE CIRCUIT ELEMENTS FOR THE PLATINUM (PT), PT BLACK, TITANIUM NITRIDE (TIN), PEDOT/TFB, PEDOT/CNT AND PEDOT/$\boldsymbol{LiClO_4}$

Electrode type	$C_{dl}(\Omega.um^2)$	$R_{CT}(F.um^2)$	**n**
Pt **[21]**	2,72 $\times 10^{-13}$	4,48 $\times 10^{12}$	0.92
$PtBlack$ **[21]**	2,08 $\times 10^{-13}$	5,11 $\times 10^{11}$	0.91
TiN **[21]**	2,03 $\times 10^{-11}$	3,00 $\times 10^{12}$	0.91
$PEDOT/TFB$ **[22]**	1,07 $\times 10^{-10}$	1,71 $\times 10^{14}$	0.96
$PEDOT/CNT$ **[16]**	6,72 $\times 10^{-11}$	3,54 $\times 10^{12}$	0.87
$PEDOT/LiClo_4$ **[20]**	1,33 $\times 10^{-9}$	2,87$\times 10^{10}$	1

VII. APPENDIX II

The transfer function of the ETI circuits presented in Figure 2.A and 2.B are computed as follows:

$$H(f) = \frac{1}{1 + j2\pi f Z_{electrode} C_s} \tag{10}$$

Where C_s is the shunt capacitance of the system due to the connectors and wires to the amplifier. It has values that range between $10pF$ to $100nF$ [11]. $Z_{electrode}$ is the total impedance of the electrode and is depicted in equations 11 and 12 for the metal electrodes (equivalent circuit in Figure 2.A) and for the coated electrodes (equivalent circuit in Figure 2.B respectively.

$$Z_{electrode}(f) = R_s + \frac{R_{CT}}{1 + R_{CT}(j2\pi f C_{dl})^n} \tag{11}$$

$$Z_{electrode}(f) = R_s + \frac{1}{j2\pi f C_d + \dfrac{1}{R_{CT_{Poly}} + Z_{Poly}}} \tag{12}$$

ACKNOWLEDGMENT

M. Al Harrach was funded by the French research agency (01/10/2019, 30/09/2020, N° ANR-18-CE19-0013-01).

REFERENCES

[1] A. S. Galanopoulou et al., “Identification of new epilepsy treatments: issues in preclinical methodology,” *Epilepsia*, vol. 53, pp. 571–582, Mar. 2012.

[2] A. Bragin et al., “High-frequency oscillations in epileptic brain,” *Current opinion in neurology*, vol. 23, pp. 151–156, Apr. 2010.

[3] S. Burnos et al., “The morphology of high frequency oscillations (HFO) does not improve delineating the epileptogenic zone,” *Clinical Neurophysiology: Official Journal of the International Federation of Clinical Neurophysiology*, vol. 127, pp. 2140–2148, Apr. 2016.

[4] S. Lee et al., “DC shifts, high frequency oscillations, ripples and fast ripples in relation to the seizure onset zone,” *Seizure*, vol. 77, pp. 52–58, Apr. 2020.

[5] M. Zijlmans et al., “High-frequency oscillations as a new biomarker in epilepsy,” *Annals of Neurology*, vol. 71, no. 2, pp. 169–178, 2012.

[6] K. A. González Otárula et al., “High-Frequency Oscillation Networks and Surgical Outcome in Adult Focal Epilepsy,” *Annals of Neurology*, vol. 85, pp. 485–494, Apr. 2019.

[7] “High-frequency oscillations mirror severity of human temporal lobe seizures,” vol. 6, pp. 2479–2488, Nov. 2019.

[8] C. Haegelen et al., “High-frequency oscillations, extent of surgical resection, and surgical outcome in drug-resistant focal epilepsy,” *Epilepsia*, vol. 54, no. 5, pp. 848–857, 2013.

[9] J. Jacobs et al., “High-frequency electroencephalographic oscillations correlate with outcome of epilepsy surgery,” *Annals of Neurology: Official Journal of the American Neurological Association and the Child Neurology Society*, vol. 67, no. 2, pp. 209–220, 2010.

[10] N. Roehri et al., “What are the assets and weaknesses of HFO detectors? A benchmark framework based on realistic simulations,” *PLoS ONE*, vol. 12, Apr. 2017.

[11] W. C. Stacey et al., “Signal distortion from microelectrodes in clinical EEG acquisition systems,” *Journal of Neural Engineering*, vol. 9, p. 056007, Aug. 2012.

[12] C. Boehler et al., “Nanostructured platinum grass enables superior impedance reduction for neural microelectrodes,” *Biomaterials*, vol. 67, pp. 346–353, Oct. 2015.

[13] W. C. Stacey et al., “Potential for unreliable interpretation of EEG recorded with microelectrodes,” *Epilepsia*, vol. 54, pp. 1391–1401, Aug. 2013.

[14] M. R. Abidian et al., “Experimental and theoretical characterization of implantable neural microelectrodes modified with conducting polymer nanotubes,” *Biomaterials*, vol. 29, pp. 1273–1283, Mar. 2008.

[15] K. Wang et al., “High-performance graphene-fiber-based neural recording microelectrodes,” *Advanced materials*, vol. 31, no. 15, p. 1805867, 2019.

[16] S. Chen et al., “PEDOT/MWCNT composite film coated microelectrode arrays for neural interface improvement,” *Sensors and Actuators A: Physical*, vol. 193, pp. 141–148, Apr. 2013.

[17] T. D. Kozai et al., “Chronic in vivo evaluation of PEDOT/CNT for stable neural recordings,” *IEEE transactions on bio-medical engineering*, vol. 63, Jan. 2016.

[18] S. Venkatraman et al., “In Vitro and In Vivo Evaluation of PEDOT Microelectrodes for Neural Stimulation and Recording,” *IEEE Transactions on Neural Systems and Rehabilitation Engineering*, vol. 19, pp. 307–316, June 2011.

[19] A. S. Pranti et al., “PEDOT: PSS coating on gold microelectrodes with excellent stability and high charge injection capacity for chronic neural interfaces,” *Sensors and Actuators B: Chemical*, vol. 275, pp. 382–393, Dec. 2018.

[20] J. Yang and D. C. Martin, “Microporous conducting polymers on neural microelectrode arrays: II. Physical characterization,” *Sensors and Actuators A: Physical*, vol. 113, pp. 204–211, July 2004.

[21] W. Franks et al., “Impedance characterization and modeling of electrodes for biomedical applications,” *IEEE Transactions on Biomedical Engineering*, vol. 52, pp. 1295–1302, July 2005.

[22] H. Charkhkar et al., “Chronic intracortical neural recordings using microelectrode arrays coated with PEDOT–TFB,” *Acta Biomaterialia*, vol. 32, pp. 57–67, Mar. 2016.

[23] R. A. Green et al., “Substrate dependent stability of conducting polymer coatings on medical electrodes,” *Biomaterials*, vol. 33, pp. 5875–5886, Sept. 2012.

[24] X. Cui and D. C. Martin, “Electrochemical deposition and characterization of poly (3, 4-ethylenedioxythiophene) on neural microelectrode arrays,” *Sensors and Actuators B: Chemical*, vol. 89, no. 1-2, pp. 92–102, 2003.

[25] C. Boehler et al., “Tutorial: guidelines for standardized performance tests for electrodes intended for neural interfaces and bioelectronics,” *Nature protocols*, vol. 15, no. 11, pp. 3557–3578, 2020.

[26] G. Paxions and K. Franklin, “The mouse brain in stereotaxic coordinates 2001.”

[27] F. Suzuki et al., “Morphogenetic effect of kainate on adult hippocampal neurons associated with a prolonged expression of brain-derived neurotrophic factor,” *Neuroscience*, vol. 64, no. 3, pp. 665–674, 1995.

[28] G. Paxinos and K. B. Franklin, *Paxinos and Franklin’s the mouse brain in stereotaxic coordinates*. Academic press, 2019.

[29] E. T. McAdams and J. Jossinet, “Tissue impedance: a historical overview,” *Physiological Measurement*, vol. 16, pp. A1–A13, Aug. 1995.

[30] J. E. B. Randles, “Kinetics of rapid electrode reactions,” *Discussions of the Faraday Society*, vol. 1, p. 11, 1947.

[31] S. Demont-Guignard et al., “Analysis of intracerebral EEG recordings of epileptic spikes: insights from a neural network model,” *Ieee Transactions on Bio-Medical Engineering*, vol. 56, pp. 2782–2795, Dec. 2009.

[32] S. Demont-Guignard et al., “Distinct hyperexcitability mechanisms underlie fast ripples and epileptic spikes,” *Annals of neurology*, vol. 71, no. 3, pp. 342–352, 2012.

[33] R. J. Burman et al., “Excitatory GABAergic signalling is associated with benzodiazepine resistance in status epilepticus,” *Brain: A Journal of Neurology*, vol. 142, no. 11, pp. 3482–3501, 2019.

[34] P. R. Rapp and M. Gallagher, “Preserved neuron number in the hippocampus of aged rats with spatial learning deficits.,” *Proceedings of the National Academy of Sciences of the United States of America*, vol. 93, pp. 9926–9930, Sept. 1996.

[35] P. Andersen et al., *The Hippocampus Book*. Oxford ; New York: OUP USA, 1 ed., Dec. 2006.

[36] T. J. Mitchell, “An Algorithm for the Construction of “D-Optimal” Experimental Designs,” *Technometrics*, vol. 16, May 1974. Publisher: Taylor & Francis pages = 203–210,.

[37] M. Al Harrach et al., “Long term evolution of fast ripples during epileptogenesis,” *Journal of Neural Engineering*, vol. 18, no. 4, p. 046027, 2021.

[38] V. I. Dzhala and K. J. Staley, “Transition from interictal to ictal activity in limbic networks in vitro,” *The Journal of Neuroscience: The Official Journal of the Society for Neuroscience*, vol. 23, pp. 7873–7880, Aug. 2003.

[39] A. J. Fuglevand et al., “Detection of motor unit action potentials with surface electrodes: influence of electrode size and spacing,” *Biological cybernetics*, vol. 67, no. 2, pp. 143–153, 1992.

[40] M. Al Harrach et al., “Model-guided design of microelectrodes for hfo recording,” in *2020 42nd Annual International Conference of the IEEE Engineering in Medicine & Biology Society (EMBC)*, pp. 3428–3431, IEEE, 2020.

[41] D. Robinson, “The electrical properties of metal microelectrodes,” *Proceedings of the IEEE*, vol. 56, pp. 1065–1071, June 1968.

[42] K. Wang et al., “High-Performance Graphene-Fiber-Based Neural Recording Microelectrodes,” *Advanced Materials*, vol. 31, no. 15, p. 1805867, 2019.

[43] S. F. Lempka et al., “Theoretical analysis of intracortical microelectrode recordings,” *Journal of neural engineering*, vol. 8, no. 4, p. 045006, 2011.

[44] J. W. Salatino et al., “Glial responses to implanted electrodes in the brain,” *Nature biomedical engineering*, vol. 1, no. 11, pp. 862–877, 2017.